Online-Journals.org

iJOE International Journal of Online and Biomedical Engineering

iJOE | eISSN: 2626-8493 | Vol. 22 No. 2 (2026) | OPEN ACCESS

https://doi.org/10.3991/ijoe.v22i02.58487

PAPER

Characteristics of Infill Pattern and Density Utilizing the Commercial Lattice Structure of 3D Printers for Application in 3D-Printed Insoles

Jutamanee Auysakul[1], **Satta Srewaradachpisal**[1], **Oriana De Becker**[2], **Bryce Adrian Killen**[2], **Surapong Chatpun**[3] (✉)

[1]Faculty of Engineering, Prince of Songkla University, Songkhla, Thailand

[2]KU Leuven, Leuven, Belgium

[3]Faculty of Medicine, Prince of Songkla University, Songkhla, Thailand

surapong.c@psu.ac.th

ABSTRACT

The increased prevalence of unhealthy lifestyles has led to an increase in numerous diseases, especially diabetes mellitus. Hyperglycemia causes peripheral neuropathy, which frequently results in loss of sensitivity in regions such as the plantar foot and increases the risk of diabetic foot ulceration. These ulcers are typically managed with therapeutic insoles designed to reduce plantar pressure. Conventional insoles typically consist of multiple layers of various soft materials. The concept of a 3D-printed insole is introduced in this study, especially regarding infill and infill density. The commercial lattice structures in 3D printers, such as honeycomb, rectilinear, and gyroid, with between 14% and 22% infill density, are considered in this work to study the mechanical behavior in terms of the ability to withstand compressive load and energy absorption capability. The honeycomb pattern with 22% infill density provides good results in comparison to other patterns. This study also verifies that a 3D-printed insole, featuring an optimized infill pattern and density, significantly reduces both the peak and mean plantar pressure in the hindfoot region during the midstance phase of the gait cycle, as observed in both the finite element (FE) model and experimental results. Significantly, this study provides guidelines on the characteristics of energy absorption and the compressive load of infill pattern and density for the 3D-printed structure to develop the orthotic insole in future studies.

KEYWORDS

infill pattern, relative density, energy absorption, 3D-printed insole, finite element (FE) analysis

1 INTRODUCTION

Custom insoles are important foot orthoses that support various biomechanical functions of the foot by providing tailored support, pressure redistribution, and enhanced comfort during movement. Traditional custom insoles are fabricated using

Auysakul, J., Srewaradachpisal, S., Becker, O. D., Killen, B. A., Chatpun, S. (2026). Characteristics of Infill Pattern and Density Utilizing the Commercial Lattice Structure of 3D Printers for Application in 3D-Printed Insoles. *International Journal of Online and Biomedical Engineering (iJOE)*, 22(2), pp. 55–75. https://doi.org/10.3991/ijoe.v22i02.58487

Article submitted 2025-09-01. Revision uploaded 2025-11-04. Final acceptance 2025-11-26.

foam cutting and injection moulding methods [1]. However, these methods often involve homogeneous structures that lack appropriate distribution of stiffness and deformation behavior. Due to the homogeneity of insole designs, the effectiveness in reducing plantar pressure using such insoles may be diminished. Advancements in 3D-printed technology have enabled the fabrication of infill structures, where both infill geometry and density can be controlled without changing the outer surface of the insole's shape [2], [3], [4], [5]. The challenge was to study the mechanical behavior of the lattice structures formed by different infill geometries to achieve plantar load redistribution and ultimately enable patient-specific support profiles.

Early work on 3D-printed insoles, such as the 3D-printed multilayer lattice structure [6], closely mimicked the mechanical behavior of clinically used EVA or PORON foams. It retained consistent stiffness across varying thicknesses, forming a lattice that conformed to standard insole design. Concurrently, the 3D-printed triangular infill pattern studied by Teixeira et al. [7] was tested under ASTM D575 to study the compression behavior for different infill densities. The combination of lower mesh density in the middle and higher mesh density in the periphery was then used for the printed heel zone inserts. The result of the dynamics impact test demonstrated its capability to absorb the impact load.

Beyond lattice topology, infill pattern and density remain the critical control variables. The five common patterns, including gyroid, grid, honeycomb, triangle, and cubic, have been employed at infill densities between 14 and 20% in [8] to study the altered energy and pressure distribution. At the same infill density, the honeycomb pattern exhibited the highest energy absorption, calculated from the area under the curve according to ASTM D575-91 [9]. The honeycomb pattern with 20% infill density reduced hindfoot pressure by 10% when compared to walking without a flat insole but modestly increased loads in the midfoot and forefoot. Concurrently, the results of the triangle, the rectilinear, and the gyroid pattern with 25%, 40%, and 60% infill densities provided better compressive modulus and strength when compared with the cubic pattern [10]. The 3D-printed gyroid pattern in [11] has high energy absorption for the orthotic insole when compared with a solid structure, whereas higher infill densities increased stiffness, potentially beyond therapeutic targets.

Parametric modelling frameworks have been developed to harness these mechanical insights for use in the simulation of real-life scenarios. The flat custom insole with different designs of infill patterns, such as hexagonal, elliptical, and circular, uses the EUP40 filament for fabrication [12]. Those insole models were integrated into the finite element (FE) model under the condition of body mass index (BMI) and activity requirement, demonstrating that the infill structure can increase energy absorption and reduce plantar pressure. Similarly, Zhang et al. [13] proposed auxetic and non-auxetic infill patterns with an average 23% infill density, fabricated from thermoplastic polyurethane (TPU), to compare the peak plantar pressure during walking and running scenarios. Their FE models showed that the auxetic 60° structure significantly reduced plantar pressure by 19.68–55.25% and increased the contact area when compared with the non-auxetic 90° structure. The FE modelling approach proved efficient for evaluating insole designs across different materials and activity conditions, saving both time and cost in the production process [14], [15], [16].

Collectively, these studies underscore that optimizing custom 3D-printed insoles demands consideration of both the infill pattern and density. The infill pattern governs the uniform stress distribution in the local area, while density dictates global stiffness. The infill patterns and densities of 3D printed structures fabricated by commercial 3D printers with slicing software could save time in manufacturing compared to traditional processes for custom insoles. While 3D-printing has become a promising technology in insole fabrication, little is known about how specific infill characteristics (pattern and density) affect plantar pressure distribution and foot healthcare outcomes. This study aims to better understand how different infill patterns and densities affect the material behavior and energy absorption under compressive loading through computational and experimental studies. Our study hypothesised that honeycomb, rectilinear, and gyroid infill patterns with 14–22% infill density would significantly reduce plantar pressure and improve comfort. This study validated the optimized 3D-printed lattice structures using FE models under compression testing standards (ASTM D575-91). This test demonstrated that energy absorption in each considered infill pattern and density could be employed for pressure redistribution in insoles. The optimized infill parameters were then used to fabricate a flat insole aimed at reducing peak plantar pressure.

2 MATERIALS AND METHODS

2.1 Workflow design for the 3D-printed insole

The conceptual framework of this study employed the mechanical properties of infill patterns in 3D printing for fabricating custom insoles using TPU. The detailed procedure for optimizing the infill pattern and simulation presented in this study is shown in Figure 1.

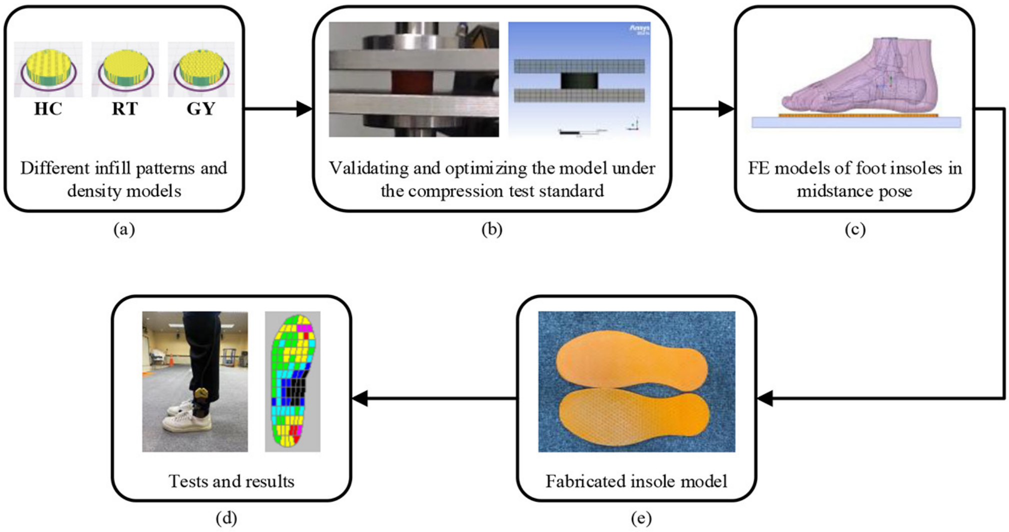

Fig. 1. Schematic representation of the methodology used within the study, where (a) shows the different infill patterns implemented; (b) optimization and validation of infill "cylinder" models; (c) finite element model of foot and insole in mid-stance pose; (d) 3D-printed flat insoles; and (e) the individual's plantar pressure measurement and results

The simulated infill patterns include honeycomb (HC), rectilinear (RT), and gyroid (GY) lattices. To compare the compression load, densities in the range of 14–22% were adopted. The 3D FE analysis was performed using the ANSYS Explicit Dynamics module (2023 R1, ANSYS Inc., USA) for simulation modelling. The explicit formulation is a dynamic simulation approach that focuses on short periods of rapid material deformation or failure. This ANSYS module controls the environment and physics of highly complex and nonlinear problems, ensuring simulations are run under quasi-static conditions. The module calculates the solver based on energy summaries at small-time increments and is superior to the static structure module due to its greater efficiency in handling self-contact interactions, particularly in lattice structures [17]. Simulation reported energy absorption data to evaluate the cushioning effect under the ASTM D575-91 testing standards. It showed the behavior of the lattice structure under both elastic and plastic deformation. The validated "cylinder" model of the infill pattern and density was then applied to the 3D-printed insole.

Plantar pressure during walking serves as an important indicator for detecting abnormalities in gait kinetics, with broad applications in conditions such as diabetic foot, knee injuries, and neuromuscular disorders [18], where impaired gait cycles reflect compromised human locomotion [19]. In this work, peak and mean plantar pressures were included in both the simulation and experimental results during the mid-stance phase of walking. To be classified as moderate for a custom insole, the peak plantar pressure was required to remain below 200 kPa [20], [21], [22].

2.2 Material properties

The material of the lattice structure in this study was assigned as TPU, which is suitable for use in 3D printing. It possesses high durability and flexibility. Moreover, TPU is considered to exhibit hyper-elastic behavior. In computational modelling, the Mooney–Rivlin model is widely used as a hyper-elastic material model [23]. It was expressed in the polynomial form of the strain energy potential. The strain energy function of the two-term Mooney–Rivlin model (W) was expressed by:

$$W = C_{10}(\bar{I}_1 - 3) + C_{01}(\bar{I}_2 - 3) + \frac{1}{d}(J - 1)^2 \tag{1}$$

Where, $\bar{I}_1$ and $\bar{I}_2$ are the first and second strain invariants of the Cauchy-Green deformation tensor, respectively. C_{10} and C_{01} represent the material constant. Then, d and J denote the incompressibility property in the material and the elastic deformation gradient, respectively. For incompressible materials, such as TPU, J equals 1. Therefore, Eq. (1) was rewritten as an infinite series for incompressible hyper-elastic behavior as shown in Eq. (2).

$$W = \sum_{i,j=0}^{N\to\infty} C_{ij}(\bar{I}_1 - 3)^i(\bar{I}_2 - 3)^j \tag{2}$$

The ANSYS software allows for curve fitting using experimental data from the uniaxial test. The uniaxial test, conducted under the ASTM D575-91 standard, used five TPU 3D-printed specimens with 100% infill density. The median stress–strain relationship from the test specimens was used to determine the material properties. The Mooney-Rivlin material constants in the third parameter ($N = 3$), C_{10}, C_{01}, and C_{11}, were extracted as –0.516 MPa, 3.92 MPa, and 0.1053 MPa, respectively. The incompressibility parameter D_1 was assigned a value of 10^{-3} MPa for fully incompressible simulations [24].

Furthermore, the material properties of other model components in this study, such as the top and bottom plates in the compression test and the soft tissue, bones, and ground in the mid-stance load scenario for the plantar pressure test, were defined as linear and homogeneous. Details on the material properties of each component were provided in Table 1.

Table 1. Material properties in the FE model

Part Name	Young's Modulus (MPa)	Poisson's Ratio
Top and bottom plate (stainless steel)	200,000	0.30
Ground plate [25]	17,000	0.10
Encapsulated soft tissue [26]	0.15	0.45
Bone [27], [28]	7,300	0.30

2.3 Specimen characteristics

The specimen in the simulation consisted of three infill patterns, including honeycomb, rectilinear, and gyroid lattice structures, with infill densities ranging from 14–22%. Previous studies [8], [10]–[11] have provided this infill density range, which significantly reduces plantar pressure and improves comfort. The commercial lattice patterns were available in the slicing software (ideaMaker software, version 5.0.5). The dimensions of the specimen are detailed in Table 2 and were fabricated using Fused Deposition Modelling (FDM) printing technology [29], [30], [31].

Table 2. Lattice structure dimensions of the TPU specimens

Infill Pattern	Infill Thickness (mm)	Infill Density		
		14%	18%	22%
Honeycomb	0.6	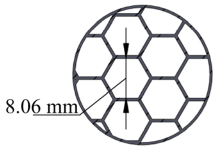	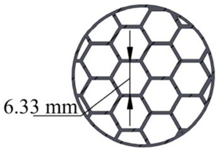	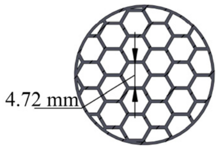
Rectilinear	0.30	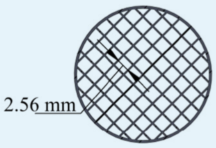	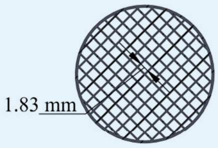	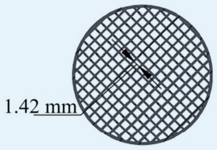
Gyroid	0.30	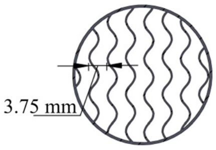	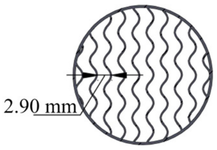	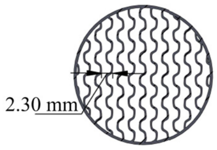

The cylindrical specimen model was shelled with a thickness of 0.4 mm to reduce the wall thickness effect under compression loading and to account for the very thin outer layer created during 3D printing. Additionally, the wall thickness of the lattice cells depends on the default settings generated by the 3D printer. Due to the thin walls of the lattice cells, ANSYS processed the 3D models by meshing with tetrahedral elements sized between 0.5 and 0.1 mm to increase the accuracy of the simulation and to achieve better solution convergence.

2.4 Compression load and boundary conditions

The insole was inserted into the shoe to absorb the plantar pressure load during the gait cycle. The distributed load from the plantar foot was applied to the insole through compressive behavior. It was therefore necessary to examine the different lattice structures of the insole under compressive loading to evaluate their mechanical characteristics, such as deformation and stress. The standard compression test was performed under ASTM D575-91 to study the stress and strain characteristics of various infill patterns and densities. The standard test specimen was shaped as a cylindrical sample with a diameter of 28.6 ± 0.1 mm and a thickness of 12.5 ± 0.5 mm. The test method involved applying compressive force at a rate of 12 ± 3 mm/min until the desired 50% strain was obtained.

To set up the FE model in the ANSYS Explicit Dynamics module, we placed the TPU specimen between the bottom and top plates, as shown in Figure 2. The bottom plate was fixed, and the top plate moved down to 6.25 mm, equal to 50% compressive strain. The bonded contact was used between the plate and the specimen (refer to Table S1). These boundary conditions were designed to mimic the real-condition test for ASTM D575-91.

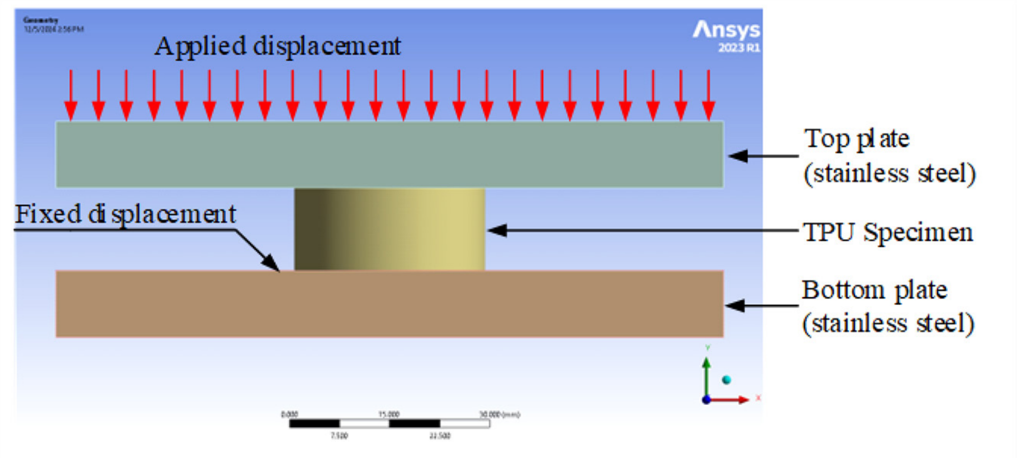

Fig. 2. Boundary conditions for the compression test

2.5 Specimen and insole printing

In this work, the Raise3D Pro2 Plus 3D printer (Raise 3D Technologies Inc., California, the United States) was used for specimen printing, and the ideaMaker software (version 5.0.5) was used for model slicing and generating the sliced G-code file to print the specimens and insole. The 3D printing process used TPU filament with Shore A95. The nozzle displacement accuracy of the device was set to 2, 2, and 0.5 μm on the x, y, and z axes, respectively, with a printing precision of 0.1 mm. The layer thickness was set to 0.2 mm. To fabricate the specimens, the infill pattern and density were selected in the slicing software (refer to Tables S2 and S3). Each infill pattern–density combination was tested using three TPU specimens (n = 3).

2.6 Boundary and loading conditions of the mid-stance gait cycle

The mid-stance phase of the gait cycle was used in this simulation scenario to compare plantar pressure with and without an insole during walking. The individual used for the load condition in this FE model was a female, 1.53 m tall, weighing 53 kg with a foot length of 230 mm. To construct the foot-insole model, the FE model was built using four components: the encapsulating soft tissues of the foot, bones, insole, and ground. These components were assembled in SolidWorks (version 2021, SolidWorks Corp., Waltham, MA, the United States), and the model was then imported into ANSYS. The FE model and boundary condition setup for the mid-stance phase are shown in Figure 3. The bone was embedded in a volume of encapsulated soft tissue, and the bones in the toe region were removed to reduce the number of fine mesh elements. All material properties used in the foot-insole model are listed in Table 1. In this study, a digital foot and bone model was obtained from the Free3D website (TurboSquid, Inc., the United States). This approach allowed us to concentrate on investigating the effects of 3D-printed insole designs, particularly the infill pattern and density, on plantar pressure reduction. By using a traditional model, the computational cost and time were reduced while maintaining the biomechanical structure. Future studies could explore subject-specific foot geometries to enhance personalization, especially for patients with diabetes. Moreover, the foot model was adjusted to the same length as the subjects. This adjustment ensured that the foot model was made to fit with the subject and the insole designs for the simulation.

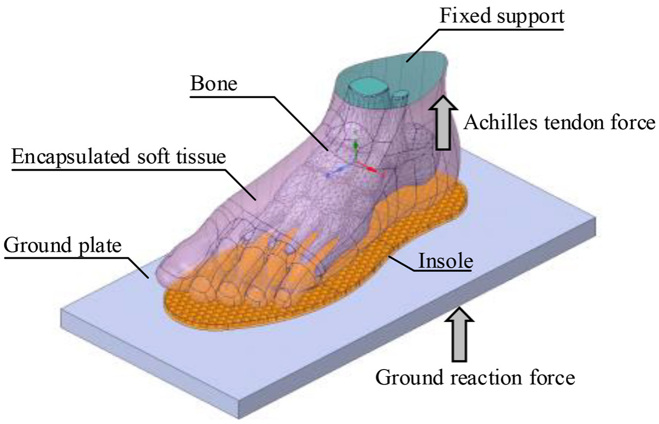

Fig. 3. FE model of the foot-insole and boundary setup

To simulate the mid-stance phase, the upper surface of the foot and bones was fixed, and the loads were applied using explicit dynamic loading with nonlinear large deformation. For the walking mid-stance simulation, the vertical ground reaction force and the Achilles tendon force were 406 N (78% of body weight) and 424 N (81.5% of body weight), respectively [32]. A coefficient of friction ($\mu = 0.6$) was used between the foot and insole, as well as between the insole and ground plate [15]. The mesh size of the ground plate was set to 8 mm, while the mesh sizes of the foot and insole ranged from 0.5 to 3 mm after refinement (details in Table S4). The insole shape was designed to fit the subject's foot, with a thickness of 5 mm, and the shelled insole had an inner thickness of 0.5 mm. The optimized infill pattern and density, determined from the test specimen simulation, were applied to the lattice structure of the 3D-printed insole to evaluate its plantar pressure distribution and energy absorption capability in comparison to the condition without an insole.

2.7 Plantar pressure measurements

Plantar pressure measurements were performed with the Pedar® system (Novel GmbH, Munich, Germany), in-shoe pressure sensors. The Pedar® system has 99 pressure sensors arranged in the shape of an insole, with a pressure range of 15–1,200 kPa, and data were collected at a frequency of 100 Hz during the measurement. Following the manufacturer's manual guideline, the Pedar insole was calibrated and set to zero before starting each test. Moreover, Pedar® software enabled tools for data analysis for each measurement and automatically calculated the average and standard deviation of several parameters, such as the plantar pressure, the peak pressure, the maximum force, and contact area for each trial. In this work, the collected data was exported and analyzed in Excel files to investigate the plantar pressure in the mid-stance phase while walking.

3 RESULTS AND DISCUSSION

3.1 Compression test

Compression tests were conducted under the ASTM D575-91 standard using a Zwick Roell machine (Ulm, Germany), as shown in Figure 4(a). A 10 kN load cell was applied at a speed of 12 mm/min. The maximum compression displacement reached 6.25 mm, corresponding to 50% strain. The TPU specimen included three samples for each of the nine models used in the infill pattern and density testing, as shown in Table 2. 3D-printed specimens with different infill patterns are shown in Figure 4(b).

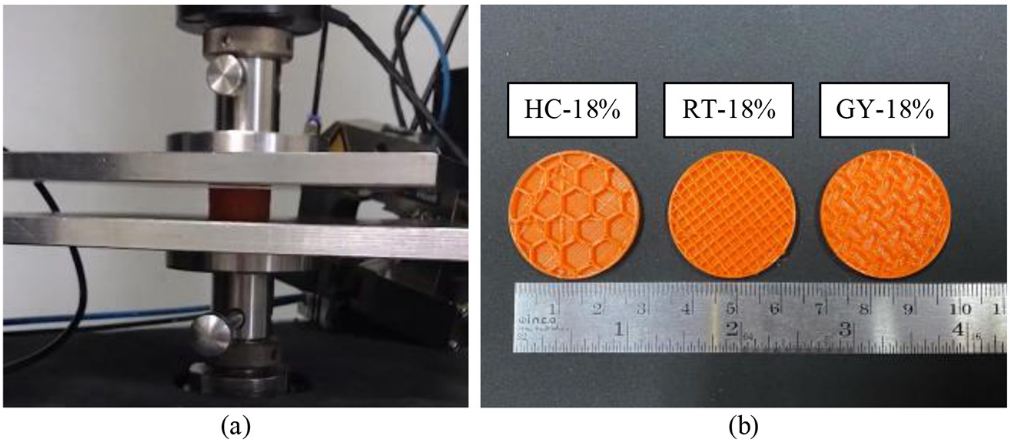

Fig. 4. (a) Testing machine and (b) examples of the TPU specimens (HC: honeycomb, RT: rectilinear and GY: gyroid)

The stress (σ)-strain (ε) curve illustrates the material's behavior when a compressive load is applied. This relationship between the two parameters provided the strength and stiffness characteristics of the material. Figure 5 shows the stress-strain curves of nine models using the median values of the specimens. The normal behavior of the specimen under compressive loading was separated into three stages: (i) linear region, (ii) plateau region, and (iii) densification region. A comparison of the specimen deformation in the experiment and simulation, showing the example of the honeycomb pattern with 22% infill density, is presented in Table 3.

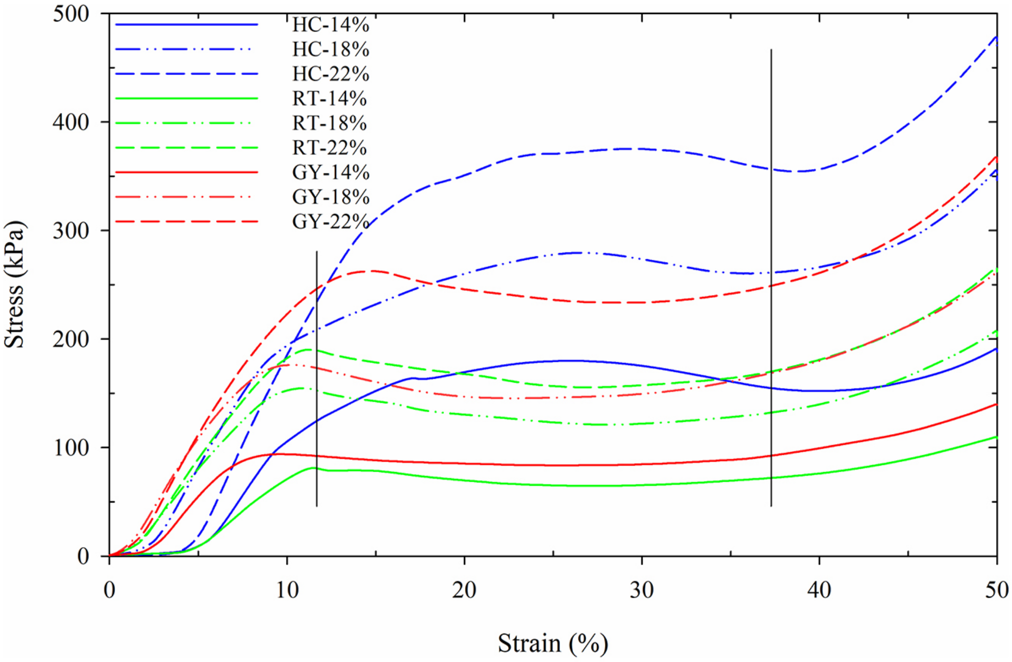

Fig. 5. Stress-strain curves from the experiment showing the different infill patterns and densities. The stress-strain curve consists of three stages: (i) linear region, (ii) plateau region, and (iii) densification region

In stage (i), the linear elastic response continued until the peak compressive load was reached; the shell wall also remained flat, and the lattice structure absorbed more energy before failing at the peak load. The structure subsequently failed when the core became unstable in stage (ii), while the curve slope exhibited a very slow stress rate compared with the strain rate due to the buckling of the vertical walls. Moreover, the stress peak was instantly reached again in stage (iii) due to structure crushing, with almost the entire structure becoming compacted. The behavior exhibited in stages (ii) and (iii) was referred to as plasticity and began when the material was stressed beyond its yield point.

As expected, increasing the infill density in each infill pattern resulted in higher maximum stress and modulus, which meant the structure stiffness increased. This effect was attributed to the increased density and larger internal volume of the specimen, which resulted in greater resistance when the plate applied a load on top of it. As mentioned previously, most experimental studies found that deformations in the simulation usually started at the top of the sample near the indenter [17], [33], [34]. This finding was consistent with our simulation results shown in Table 3.

Table 3. Comparison of the honeycomb, rectilinear, and gyroid specimens with 22% infill density and deformation in different stages

Compression	Experiment	Deformation in Simulation*		
		Honeycomb	Rectilinear	Gyroid
Stage (i) linear region	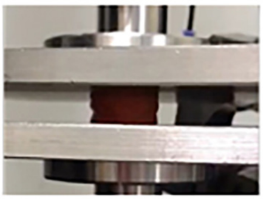	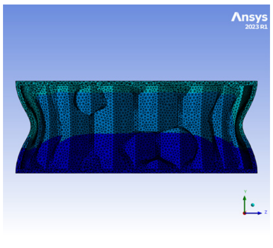	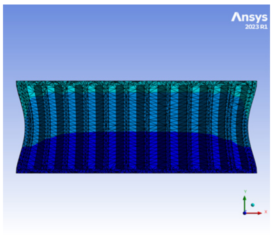	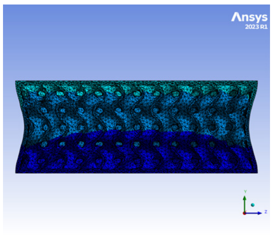
Stage (ii) plateau region	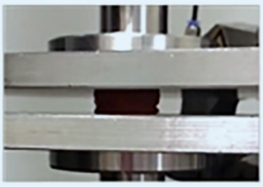	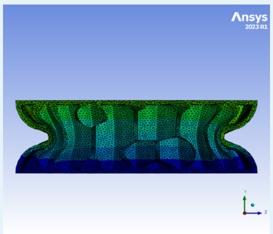	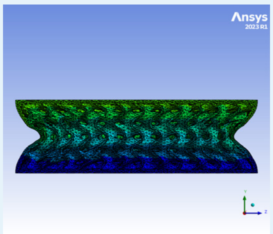	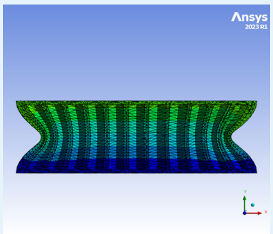
Stage (iii) densification region	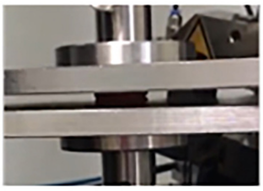	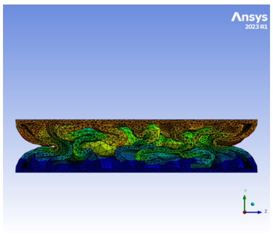	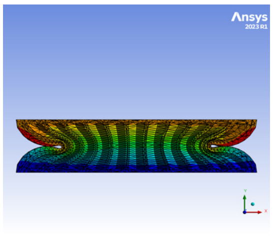	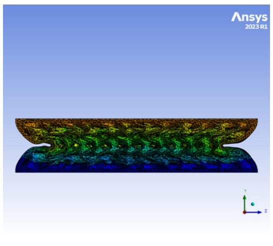
*Deformation contour				

Increasing the relative density in the lattice structure improved the compressive strength. The stress–strain curves of TPU specimens with different infill densities showed a similar pattern in the three stages of deformation, just like in other studies. This similarity persisted despite the use of different lattice structures during the compression tests, as demonstrated in the works of Teixeira et al. [7] and Kumar et al. [35], which created triangular mesh and spiderweb structures, respectively, for the lattice design. The relative density of the lattice structure had a positive effect on the compressive strength of TPU.

The energy absorption ability of the TPU lattice structure is illustrated in Figure 6 (refer to Tables S5 and S6). The energy absorption was calculated from the area under the load curve based on the stress–strain relationship. In the elastic zone, the energy absorption capability increased significantly from 14% to 22% infill densities due to a rise in the number of lattice cells, with similar values observed at 18% and 22% infill densities. The gyroid and honeycomb patterns demonstrated similar energy absorption in this zone at 14% and 18% infill densities, but the gyroid exhibited the highest energy absorption at 22% infill density due to its increased stiffness. However, the energy absorption capacity of the honeycomb pattern was the highest among all infill patterns in the plastic zone, as the stress behavior exceeded the material's yield point. This indicates that the honeycomb pattern has strong shock absorption capability.

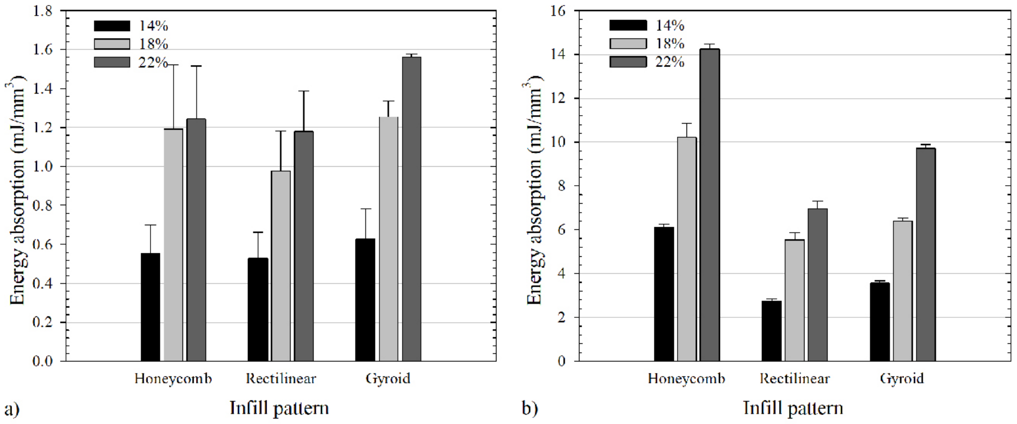

Fig. 6. Energy absorption capacity of the test specimens: (a) in the elastic zone and (b) in the plastic zone

The energy absorption increased with infill density, corresponding to the specimen's behavior under compressive load. Additionally, the honeycomb lattice structure had a greater wall area than the other patterns when compared cell by cell. As a result, the honeycomb pattern exhibited the highest stiffness among the infill patterns, followed by gyroid and rectilinear, respectively, at the same infill density, as shown in Figure 7 (refer to Table S7).

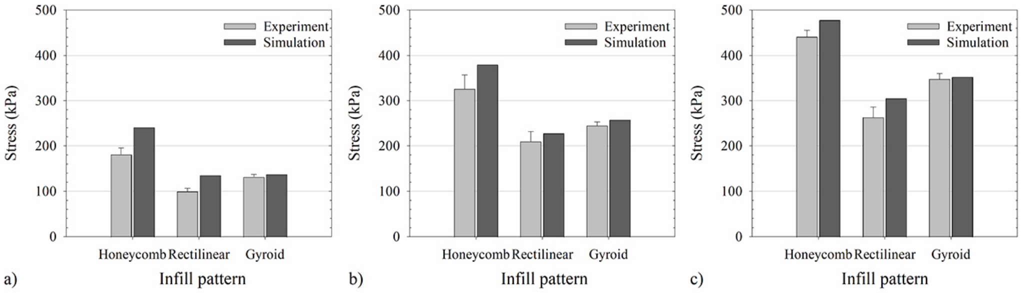

Fig. 7. Comparison of compressive stress between the experiment and simulation with different infill patterns and densities at 50% strain with infill densities (a) 14%, (b) 18%, (c) 22%

The percentage error between the simulation model and the experimental results decreased with increasing infill density. This reduction was attributed to the vertical walls in the shelled specimen becoming less influential as density increased. When compared with a previous study, the compressive strength of cubic, rectilinear, gyroid, and triangle lattices was also found to increase with infill density [10]. The compressive strength of the gyroid lattice at 25% infill density was higher than that of the rectilinear lattice, which aligned with the findings for 22% infill density in this study, as shown in Table 4.

However, the honeycomb infill pattern provided the highest maximum compressive strength compared to the other infill patterns. Therefore, the honeycomb pattern with 22% infill density was selected to fabricate a flat insole with a thickness of 5 mm, as it could withstand greater stress without failure. This enabled a detailed study of plantar pressure distribution and energy absorption effectiveness for long-term use. This combination enhanced comfort and optimized performance for individuals requiring supportive footwear. Future studies were planned to further explore the effects of varying thicknesses and materials on overall efficacy in real-world applications.

Table 4. Results of the compression test

Specimen		Stress at 50% Strain (kPa)		
Infill Pattern	**Infill Density (%)**	**Experiment**	**Simulation**	**%Error**
Honeycomb	14	181.1	240.9	33.02
	18	325.9	379.3	16.04
	22	440.9	477.5	8.31
Rectilinear	14	99.9	135.5	35.56
	18	209.8	227.9	8.63
	22	263.0	305.1	16.01
Gyroid	14	131.8	137.6	4.38
	18	245.1	257.6	5.11
	22	347.5	352.2	1.34

3.2 Comparison of plantar pressure between FE simulation and the gait experiment

To validate the FE model with experimental measurements, the Pedar® system (Novel GmbH, Munich, Germany) was employed to measure pressure distribution and calculate the reaction force using the Pedar-x Expert software (version 22.3.3, Novel GmbH, Munich, Germany). The flat insole design was preliminarily validated with a healthy adult. The subject wore Pedar insoles in EU size 37 inside the shoe midsole to monitor the loads between the foot and ground plate, as shown in Figure 8(a). Plantar pressure data was collected while the subject walked 10 m at a self-selected speed (average 1.67 steps/m) on a flat and straight path, as shown in Figure 8(b). This distance was sufficient to record gait cycles for the study. The experiment was conducted at the Southern Medical Rehabilitation Centre of Songklanagarind Hospital.

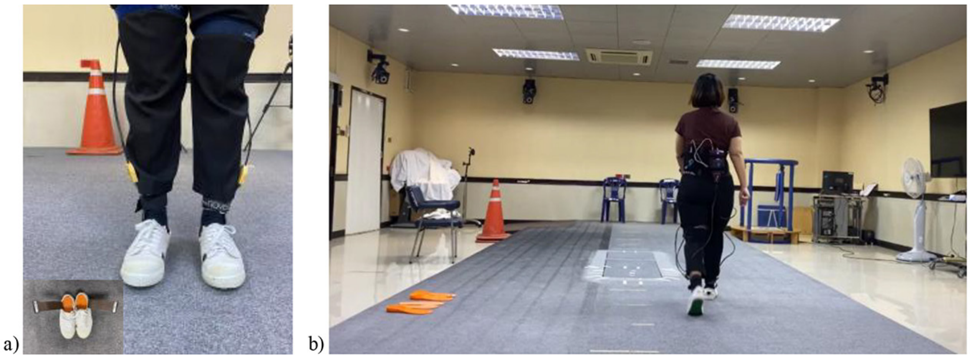

Fig. 8. (a) Pedar insole system setup and (b) experiment showing the walking path to measure gait data

To compare the distribution of peak and mean plantar pressure during the mid-stance phase of walking, the plantar pressure area was divided into three regions: the hindfoot (HF), midfoot (MF), and forefoot (FF), as shown in Figure 9(a). High plantar pressure was observed in the heel area of the hindfoot region and in the medial and lateral areas of the forefoot region. This pressure distribution occurred during the mid-stance phase in both experimental and simulation results, as illustrated in Figure 9(b) and (c), respectively. It was essential for the plantar pressure to be concentrated in these two regions, as they were the most susceptible to ulceration in diabetic feet. The experimental results were averaged from 15 gait cycles during the mid-stance phase to compare the plantar pressure distribution with that of the FE model.

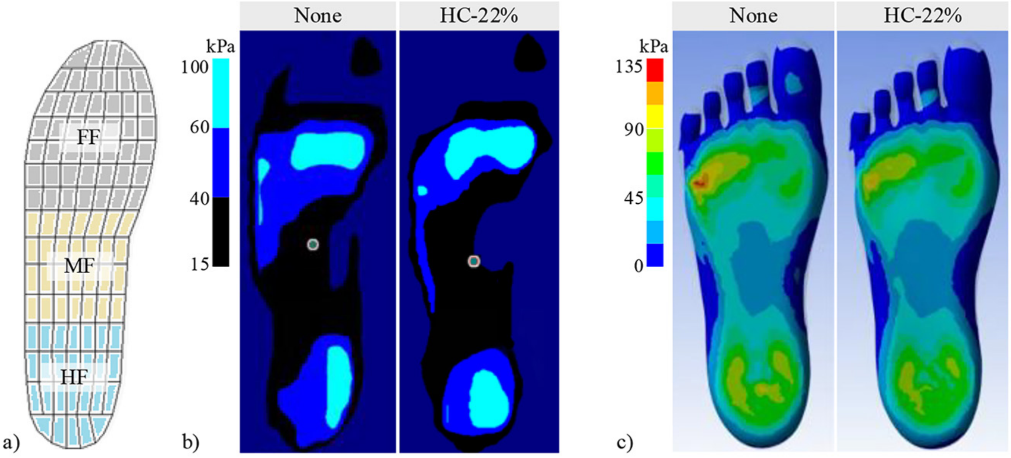

Fig. 9. (a) Schematic showing the plantar regions of the Pedar insoles, (b) Distributions of mean plantar pressure from the Pedar® system, and (c) Distribution of peak plantar pressure in simulation in case of without and with a flat insole with 22% infill density and honeycomb (HC) infill pattern

Figure 10 illustrates the plantar pressure in terms of peak and mean values across each region (refer to Tables S8 and S9). The honeycomb pattern with 22% infill density reduced the peak plantar pressure in the hindfoot region by more than 15% and decreased the mean plantar pressure in both the simulation and experimental results compared to the condition without an insole. The hindfoot region received the impact load between the vertical force from the ground plate and the fixed support in the simulation. This indicated that the honeycomb pattern was capable of absorbing energy from the compressive load. However, the 3D-printed flat insole did not significantly reduce the peak and mean plantar pressure in the midfoot and forefoot regions. On the other hand, Shaikh et al. [36] presented a customized 3D-printed insole in the heel cup, heel rise, medial arch height, and lateral wedge, which was reported to alleviate pain for 90% of the 200 patients. Therefore, we could develop a customized 3D-printed insole based on the specific needs of various patients using the presented infill pattern from this study.

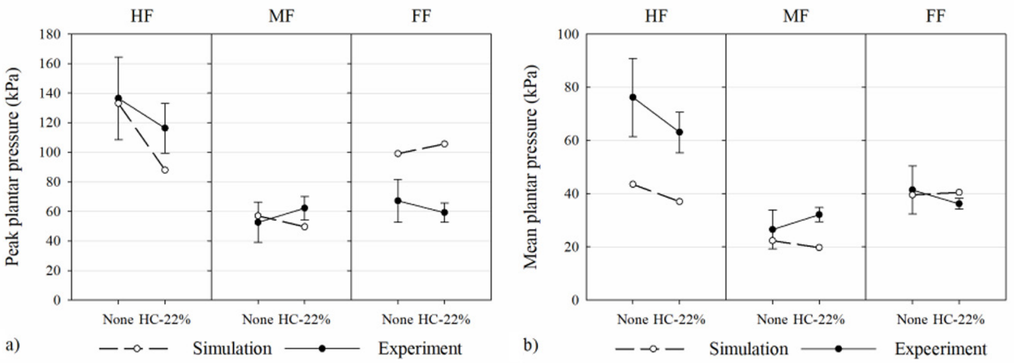

Fig. 10. Comparison of results between FE simulation and the experiment with and without the insole during the mid-stance phase: (a) peak plantar pressure and (b) mean plantar pressure

In the FE model, some discrepancies were observed when compared with the experimental measurements, particularly in the forefoot region for peak plantar pressure and the hindfoot region for mean plantar pressure. The elevated peak plantar pressure in the forefoot region in the simulation was attributed to the exclusion of bones in the toe region, a simplification made to reduce computational costs. Additionally, during the experiment, the sports shoes may have felt tight to the wearer in the hindfoot region, whereas in the simulation, the sports shoes were not included in the FE model. As a result, the mean plantar pressure in the hindfoot region was higher in the experimental results than in the simulation.

In conclusion, the FE model was able to predict the peak and mean plantar pressure with similar trends in certain areas, especially in the hindfoot, when compared to real-world conditions. It can detect and predict the relative change in pressure caused by the insole design. This change-detection capability is highly relevant for design purposes, since it allows us to evaluate whether new insole geometries can effectively reduce plantar pressure in critical regions prone to ulceration. However, the accuracy of the model remains limited by factors such as differences in the material properties of bones and soft tissue between the simulation and the actual foot, as well as the absence of anatomical structures like ligaments, the plantar fascia, and musculotendon units that apply muscle forces to move the joints. Furthermore, this study implemented the infill characteristics on the flat insole, which was a general testing concept. Therefore, it is recommended to implement with other types of insoles, such as arch support insoles.

4 CONCLUSION

This study investigated the effects of infill patterns and densities on the mechanical behaviors of 3D-printed TPU specimens. The honeycomb infill pattern was found to have the highest stiffness, followed by the gyroid and rectilinear patterns, respectively, at the same infill density. This was due to the honeycomb structure having a greater wall area compared to the other patterns when assessed cell by cell. The honeycomb infill pattern also demonstrated superior energy absorption capability in both the elastic and plastic deformation regions. The optimized and validated model had a honeycomb structure with a 22% infill density, which was subsequently used to fabricate the 3D-printed flat insole. The peak plantar pressure in the hindfoot region was reduced by more than 15% when wearing the 3D-printed flat insole, compared to walking without it, as observed in both the experimental testing system and the FE model during the mid-stance phase. However, the 3D-printed flat insole did not produce significant reductions in plantar pressure in the midfoot and forefoot regions. Thus, this study suggested that future insole designs using a honeycomb infill pattern could potentially reduce plantar pressure loads and the risk of ulceration in diabetic feet, particularly in the hindfoot region. Furthermore, it is recommended that future research should explore the development of 3D-printed insoles specifically designed for therapeutic shoes intended for individuals with diabetic foot conditions.

5 FUNDING

This study was funded by Horizon Europe Framework Program under Grant No. 101086348.

6 SUPPLEMENTARY MATERIALS

Supplementary materials for this article are available.

7 DATA AVAILABILITY STATEMENT

The authors confirm that the data supporting the findings of this study are available within the article and its supplementary materials.

8 REFERENCES

[1] R. A. Hanly, "Improvements in the production of nonwoven shoe insole fabrics," Ph.D. thesis, University of Leeds, 2023.

[2] L. P. Kang and T. S. Gong, "Design of 3D printed pressure-reducing insoles based on changes in parameters of lattice structure," *Advances in Mechanical Engineering*, vol. 15, no. 12, pp. 1–11, 2023. https://doi.org/10.1177/16878132231216609

[3] S. Jandova and R. Mendricky, "Benefits of 3D printed and customized anatomical footwear insoles for plantar pressure distribution," *3D Printing and Additive Manufacturing*, vol. 9, no. 6, pp. 547–556, 2022. https://doi.org/10.1089/3dp.2021.0002

[4] M. Ntagios and R. Dahiya, "3D printed soft and flexible insole with intrinsic pressure sensing capability," *IEEE Sensors Journal*, vol. 23, no. 20, pp. 23995–24003, 2022. https://doi.org/10.1109/JSEN.2022.3179233

[5] A. Daryabor, T. Kobayashi, H. Saeedi, S. M. Lyons, N. Maeda, and S. S. Naimi, "Effect of 3D printed insoles for people with flatfeet: A systematic review," *Assistive Technology*, vol. 35, no. 2, pp. 169–179, 2023. https://doi.org/10.1080/10400435.2022.2105438

[6] K. A. Nickerson, E. Y. Li, S. Telfer, W. R. Ledoux, and B. C. Muir, "Exploring the mechanical properties of 3D-printed multilayer lattice structures for use in accommodative insoles," *Journal of the Mechanical Behavior of Biomedical Materials*, vol. 150, p. 106309, 2024. https://doi.org/10.1016/j.jmbbm.2023.106309

[7] R. Teixeira *et al.*, "Towards customized footwear with improved comfort," *Materials*, vol. 14, no. 7, p. 1738, 2021. https://doi.org/10.3390/ma14071738

[8] S. Chatpun, T. Dissaneewate, A. Kwanyuang, M. Nouman, S. Srewaradachpisal, and D. Movrin, "Infill pattern and density of 3D-printed insoles alter energy and pressure distribution in Gait," *Applied Sciences*, vol. 15, no. 7, p. 3916, 2025. https://doi.org/10.3390/app15073916

[9] ASTM International, *Standard Test Methods for Rubber Properties in Compression*. ASTM D575-91, West Conshohocken, PA, 2002.

[10] B. Orsu and Y. P. Shaik, "Compression strength analysis of customized shoe insole with different infill patterns using 3D printing," *Open Access Library Journal*, vol. 9, no. 5, pp. 1–13, 2022. https://doi.org/10.4236/oalib.1108712

[11] U. K. Jonnala and Y. R. Kumar, "Design and development of fused deposition modeling (FDM) 3D-Printed Orthotic Insole by using gyroid structure," *Journal of the Mechanical Behavior of Biomedical Materials*, vol. 145, p. 106005, 2023. https://doi.org/10.1016/j.jmbbm.2023.106005

[12] A. Zolfagharian, M. Lakhi, S. Ranjbar, and M. Bodaghi, "Custom shoe sole design and modeling toward 3D printing," *International Journal of Bioprinting*, vol. 7, no. 4, p. 396, 2021. https://doi.org/10.18063/ijb.v7i4.396

[13] J. Zhang, S. Lu, Y. Lin, Y. Wang, X. Yi, and W. Fang, "Pressure-reducing design of 3D-printed diabetic shoe midsole utilizing auxetic lattice structure," *Applied Sciences*, vol. 14, no. 12, p. 5291, 2024. https://doi.org/10.3390/app14125291

[14] H. Zhang *et al.*, "Computational modelling of foot orthosis for midfoot arthritis: A Taguchi approach for design optimization," *Acta of Bioengineering and Biomechanics*, vol. 22, no. 4, pp. 75–83, 2020. https://doi.org/10.37190/ABB-01694-2020-03

[15] Z. Yang *et al.*, "Design feature combinations effects of running shoe on plantar pressure during heel landing: A finite element analysis with Taguchi optimization approach," *Frontiers in Bioengineering and Biotechnology*, vol. 10, p. 959842, 2022. https://doi.org/10.3389/fbioe.2022.959842

[16] A. Nourani, M. D. Daei, and M. Honarmand, "Comparison of energy absorption in conventional and auxetic shoes: Gait analysis and finite element modeling," *Journal of Design Against Fatigue*, vol. 1, no. 2, 2023. htts://doi.org/10.62676/jz62m929

[17] H. Rahman, E. Yarali, A. Zolfagharian, A. Serjouei, and M. Bodaghi, "Energy absorption and mechanical performance of functionally graded soft–hard lattice structures," *Materials*, vol. 14, no. 6, p. 1366, 2021. https://doi.org/10.3390/ma14061366

[18] A. Mohd Noor, "An instrumented insole system for gait monitoring and analysis," *International Journal of Online Engineering*, vol. 10, no. 6, pp. 30–34, 2014. https://doi.org/10.3991/ijoe.v10i6.3971

[19] G. Govindaraj and A. S. A. Doss, "Evaluation of robotic ankle-foot orthosis with different actuators using simscape multibody for foot-drop patients," *International Journal of Online & Biomedical Engineering*, vol. 19, no. 10, pp. 156–168, 2023. https://doi.org/10.3991/ijoe.v19i10.40375

[20] S. Ahmed, A. Barwick, P. Butterworth, and S. Nancarrow, "Footwear and insole design features that reduce neuropathic plantar forefoot ulcer risk in people with diabetes: A systematic literature review," *Journal of Foot and Ankle Research*, vol. 13, no. 1, pp. 1–13, 2020. https://doi.org/10.1186/s13047-020-00400-4

[21] B. C. Muir, J. S. Li, Y. F. Hudak, G. E. Kaufman, S. Cullum, and P. M. Aubin, "Evaluation of novel plantar pressure-based 3-dimensional printed accommodative insoles – a feasibility study," *Clinical Biomechanics*, vol. 98, p. 105739, 2022. https://doi.org/10.1016/j.clinbiomech.2022.105739

[22] J. Tang *et al.*, "A wearable insole system to measure plantar pressure and shear for people with diabetes," *Sensors*, vol. 23, no. 6, p. 3126, 2023. https://doi.org/10.3390/s23063126

[23] M. R. Sheikhi, B. Shamsadinlo, O. Unver, and S. Gurgen, "Finite element analysis of different material models for polyurethane elastomer using estimation data sets," *Journal of the Brazilian Society of Mechanical Sciences and Engineering*, vol. 43, no. 12, art. no. 554, 2021. https://doi.org/10.1007/s40430-021-03279-9

[24] G. B. Raj, A. Saludheen, A. K. Arumugham-Achari, N. George, and T. Chacko, "Simulations for mechanical properties of polymer composites: investigations into suitability of numerical models for TPU-CNT with Mooney–Rivlin (N=1) and friction," *Mechanics of Time-Dependent Materials*, vol. 27, no. 3, pp. 705–726, 2023. https://doi.org/10.1007/s11043-022-09565-w

[25] J. T. M. Cheung and M. Zhang, "Parametric design of pressure-relieving foot orthosis using statistics-based finite element method," *Medical Engineering & Physics*, vol. 30, no. 3, pp. 269–277, 2008. https://doi.org/10.1016/j.medengphy.2007.05.002

[26] Y. C. Hsu *et al.*, "Using an optimization approach to design an insole for lowering plantar fascia stress—a finite element study," *Annals of Biomedical Engineering*, vol. 36, no. 8, pp. 1345–1352, 2008. https://doi.org/10.1007/s10439-008-9516-x

[27] J. Niu, J. Liu, Y. Zheng, L. Ran, and Z. Chang, "Are arch-conforming insoles a good fit for diabetic foot? Insole customized design by using finite element analysis," *Human Factors and Ergonomics in Manufacturing & Service Industries*, vol. 30, no. 4, pp. 303–310, 2020. https://doi.org/10.1002/hfm.20841

[28] Z. Taha, M. S. Norman, S. F. S. Omar, and E. Suwarganda, "A finite element analysis of a human foot model to simulate neutral standing on ground," *Procedia Engineering*, vol. 147, pp. 240–245, 2016. https://doi.org/10.1016/j.proeng.2016.06.240

[29] R. B. Kristiawan, F. Imaduddin, D. Ariawan, Ubaidillah, and Z. Arifin, "A review on the fused deposition modeling (FDM) 3D printing: Filament processing, materials, and printing parameters," *Open Engineering*, vol. 11, no. 1, pp. 639–649, 2021. https://doi.org/10.1515/eng-2021-0063

[30] K. Rajan, M. Samykano, K. Kadirgama, W. S. W. Harun, and M. M. Rahman, "Fused deposition modeling: Process, materials, parameters, properties, and applications," *The International Journal of Advanced Manufacturing Technology*, vol. 120, no. 3, pp. 1531–1570, 2022. https://doi.org/10.1007/s00170-022-08860-7

[31] A. Aljazara *et al.*, "Quality of 3D printed objects using fused deposition modeling (FDM) technology in terms of dimensional accuracy," *International Journal of Online and Biomedical Engineering*, vol. 19, no. 14, pp. 45–62, 2023. https://doi.org/10.3991/ijoe.v19i14.43761

[32] Y. N. Chen, C. W. Chang, C. T. Li, C. H. Chang, and C. F. Lin, "Finite element analysis of plantar fascia during walking: A quasi-static simulation," *Foot & Ankle International*, vol. 36, no. 1, pp. 90–97, 2015. https://doi.org/10.1177/1071100714549189

[33] X. Guo, E. Wang, H. Yang, and W. Zhai, "Mechanical characterization and constitutive modeling of additively-manufactured polymeric materials and lattice structures," *Journal of the Mechanics and Physics of Solids*, vol. 189, p. 105711, 2024. https://doi.org/10.1016/j.jmps.2024.105711

[34] R. Kumar and S. K. Sarangi, "3D Printed customized diabetic foot insoles with architecture designed lattice structures – a case study," *Biomedical Physics & Engineering Express*, vol. 10, no. 1, 2023. https://doi.org/10.1088/2057-1976/ad1732

[35] R. Kumar and S. K. Sarangi, "On the enhanced mechanical characteristics of 3D printed architected spiderweb lattice structures through overall density variation," *Engineering Research Express*, vol. 5, no. 3, 2023. https://doi.org/10.1088/2631-8695/acf981

[36] S. Shaikh, B. Jamdade, and A. Chanda, "Effects of customized 3D-printed insoles in patients with foot-related musculoskeletal ailments—a survey-based study," *Prosthesis*, vol. 5, no. 2, pp. 550–561, 2023. https://doi.org/10.3390/prosthesis5020038

9 SUPPLEMENT MATERIALS

Supplement 1: FE input for the compression load

The details for analyzing the compression load using ANSYS Workbench are provided in Table S1 for condition settings and in Table 1 for material properties.

Table S1. FE condition and analysis setting for the compressive load simulation

Category	Model/Detail	Type	Value
Mesh	Top and bottom plate	Body sizing (element size)	4.0 mm
	Specimen	Body sizing (element size)	0.1–0.5 mm
Contact	Specimen and top plate	Bonded	–
	Specimen and bottom plate	Bonded	–
Boundary condition	Bottom plate	Fixed support	
	Top plate	Displacement	–6.25 mm (y-axis)

(Continued)

Table S1. FE condition and analysis setting for the compressive load simulation *(Continued)*

Category	Model/Detail	Type	Value
Analysis setting	Step controls	Number of steps	60
	Step controls	Load step type	Explicit time integration
	Step controls	End time	6×10^{-3}
	Step controls	Maximum number of cycles	10^7
	Step controls	Maximum energy error	0.1
	Output controls	Result number of points	200
	Output controls	Restart number of points	5

Supplement 2: Slicer profiles

The slicer profiles for the specimen and the flat insole are set up according to the parameters specified in Tables S2 and S3. The supplementary STL files S1 and S2 contain the specimen model and the flat insole, which correspond to the slicer profiles found in Slicer files S1 and S2, respectively.

Table S2. Parameters declared for the ideaMaker v5.0.5 software based on the slicer settings

Parameter	Value/Definition
Height of the first layer	0.30 mm
Infill	Data in Table S6
Nozzle diameter	0.40 mm
Layer height	0.20 mm
Nozzle displacement accuracy (X/Y axis)	2 µm
Nozzle displacement accuracy (Z axis)	0.5 µm
Nozzle temperature	225 ˚C
Heated bead temperature	60 ˚C
Speed of the print head	30 mm/s
Speed of idle movement (X/Y axis)	150 mm/s
Speed for the first layer	15 mm/s

Table S3. Initial settings for the slicer software

Infill Pattern	Infill Density (%)
Honeycomb	14, 18, 22
Rectilinear	14, 18, 22
Gyroid	14, 18, 22

Supplement 3: FE input for plantar pressure in the mid-stance phase of the gait cycle

The details for analyzing the plantar pressure in the mid-stance phase of the gait cycle by employing the ANSYS Workbench are detailed in the condition setting and material properties as Table S4 and Table 1, respectively.

Table S4. FE condition and analysis setting for plantar pressure in the mid-stance phase

Category	Model/Detail	Type	Value
Mesh	Ground plate	Face sizing	8.0 mm
	Insole	Body sizing (element size)	0.3 mm
	Foot	Body sizing (sphere of influence)	2.8 mm
	Bone	Body sizing (sphere of influence)	2.0 mm
Contact	Foot and insole	Frictional	0.6
	Insole and ground plate	Frictional	0.6
Boundary condition	Top surface of foot and bone	Fixed support	
	Top surface of ground plate	Force	424 N
	Bone (Achilles tendon force)	Force	406 N
	Ground plate	Displacement	0 in x-y axis, and free in y axis
Analysis setting	Step controls	Number of steps	20
	Step controls	Load step type	Explicit time integration
	Step controls	End time	2×10^{-2}
	Step controls	Maximum number of cycles	10^7
	Step controls	Maximum energy error	0.1
	Output controls	Result number of points	100
	Output controls	Restart number of points	5

Supplement 4: Statistical values for all experimental results

Table S5. Statistical values for the energy absorption capacity of the test specimens in the elastic zone (see Figure 6(a)) with different filling patterns and densities

Sample	N	Mean	SD	95% CI for μ
HC-14%	3	0.555	0.145	(0.1956, 0.9133)
HC-18%	3	1.192	0.328	(0.378, 2.007)
HC-22%	3	1.243	0.272	(0.567, 1.919)
RT-14%	3	0.529	0.134	(0.1967, 0.8613)
RT-18%	3	0.977	0.205	(0.468, 1.486)
RT-22%	3	1.179	0.208	(0.661, 1.697)
GY-14%	3	0.627	0.157	(0.2369, 1.0180)
GY-18%	3	1.255	0.080	(1.0563, 1.4541)
GY-22%	3	1.561	0.015	(1.52346, 1.59946)

Unit: mJ/mm^3, and μ: population mean of each specimen.

Table S6. Statistical values for the energy absorption capacity of the test specimens in the plastic zone (see Figure 6(b)) with different filling patterns and densities

Sample	N	Mean	SD	95% CI for μ
HC-14%	3	6.126	0.125	(5.8144, 6.4372)
HC-18%	3	10.212	0.647	(8.604, 11.820)
HC-22%	3	14.252	0.227	(13.688, 14.816)
RT-14%	3	2.730	0.132	(2.4011, 3.0590)
RT-18%	3	5.546	0.311	(4.773, 6.318)
RT-22%	3	6.958	0.343	(6.106, 7.810)
GY-14%	3	3.572	0.092	(3.3433, 3.8008)
GY-18%	3	6.401	0.129	(6.0799, 6.7222)
GY-22%	3	9.721	0.168	(9.3028, 10.1396)

Unit: mJ/mm^3, and μ: population mean of each specimen.

Table S7. Statistical values for compression test results (see Figure 7 and refer to Table 4) with different filling patterns and densities

Sample	N	Mean	SD	95% CI for μ
HC-14%	3	181.1	14.31	(145.56, 216.67)
HC-18%	3	325.9	30.80	(249.2, 402.5)
HC-22%	3	440.9	14.58	(404.63, 477.07)
RT-14%	3	99.9	6.45	(83.91, 115.95)
RT-18%	3	209.8	21.90	(155.4, 264.2)
RT-22%	3	263.0	22.70	(206.7, 319.3)
GY-14%	3	131.8	5.43	(118.35, 145.32)
GY-18%	3	245.1	7.99	(225.24, 264.93)
GY-22%	3	347.5	12.51	(316.45, 378.62)

Unit: kPa, and μ: population mean of each specimen.

Table S8. Statistical values for peak plantar pressure plantar pressure test results (see Figure 10 (a))

Sample	N	Mean	SD	95% CI for μ
Hindfoot				
Without insole	15	136.46	27.96	(120.97, 151.94)
With insole (HC-22%)	15	116.33	16.90	(106.97, 125.69)
Midfoot				
Without insole	15	52.54	13.62	(44.99, 60.08)
With insole (HC-22%)	15	62.17	7.95	(57.76, 66.57)
Forefoot				
Without insole	15	67.12	14.53	(59.08, 75.17)
With insole (HC-22%)	15	59.17	6.59	(55.52, 62.82)

Unit: kPa, and μ: population mean of each peak plantar pressure region.

Table S9. Statistical values for mean plantar pressure plantar pressure test results (see Figure 10 (b))

Sample	N	Mean	SD	95% CI for μ
Hindfoot				
Without insole	15	76.21	14.69	(68.07, 84.34)
With insole (HC-22%)	15	63.07	7.63	(58.85, 67.30)
Midfoot				
Without insole	15	26.49	7.33	(22.43, 30.55)
With insole (HC-22%)	15	32.10	2.67	(30.627, 33.584)
Forefoot				
Without insole	15	41.40	9.02	(36.41, 46.40)
With insole (HC-22%)	15	36.20	2.10	(35.032, 37.364)

Unit: kPa, and μ: population mean of each mean plantar pressure region.

10 AUTHORS

Jutamanee Auysakul serves as an Assistant Professor at Department of Mechanical and Mechatronics Engineering, Faculty of Engineering, Prince of Songkla University, Songkhla 90110, Thailand. Her research interests are the analysis and design of mechatronic systems and finite element analysis (E-mail: jutamanee.a@psu.ac.th).

Satta Srewaradachpisal is a Lecturer and researcher at Department of Mechanical and Mechatronics Engineering, Prince of Songkla University, Songkhla 90110, Thailand. He graduated with a bachelor's degree in manufacturing engineering from Prince of Songkla University in 2008 and Master's and Ph.D. degrees in mechanical engineering from Prince of Songkla University, Thailand, in 2012 and 2021, respectively. His expertise is interested in the following areas of research: finite element analysis, applied mechanics, biomechanics, and rubber engineering (E-mail: satta.sre@gmail.com).

Oriana De Becker obtained a Master of Biomedical Engineering from KU Leuven, Belgium, in 2023. She is currently pursuing a PhD within the Biomechanics Division of the Department of Mechanical Engineering at KU Leuven. Her research interests include biomechanics, computational modelling, and the numerical simulation of bioresorbable materials (E-mail: oriana.debecker@kuleuven.be).

Bryce Adrian Killen obtained his PhD in Computational Biomechanics from Griffith University in Australia in 2019 focusing on image-based, and statistical shape modelling derived musculokskeletal models for human movement. He has been a postdoctoral research fellow at KU Leuven Belgium for 6 years focusing on the modelling of knee osteoarthritis to understand the progression and development of the disease and potential rehabilitation strategies as well as developing methods for clinical translation of lab-based methods (E-mail: bryce.killen@kuleuven.be).

Surapong Chatpun received his Ph.D. in Bioengineering from the University of California, USA, in 2010. He currently leads the Cardiovascular Engineering Research Laboratory (CERLab), Faculty of Medicine, Prince of Songkla University, Songkhla 90110, Thailand. His research focuses on applying engineering approaches, such as continuum mechanics, numerical methods (e.g., FEM), fluid mechanics (e.g., CFD), image processing, and computer-aided design, combined with life sciences knowledge and available technologies to enhance understanding of the circulatory system's function and mechanisms in both normal and pathological conditions. He also designs and invents medical devices not only for cardiovascular applications but also for other clinical areas, such as rehabilitation and orthopedics (E-mail: surapong.c@psu.ac.th).